

SYNCHROTRON SELF-ABSORPTION IN GAMMA-RAY BURST AFTERGLOW

JONATHAN GRANOT, TSVI PIRAN, AND RE'EM SARI

Racah Institute, Hebrew University, Jerusalem 91904, Israel; jgranot@nikki.fiz.huji.ac.il, tsvi@nikki.fiz.huji.ac.il, sari@nikki.fiz.huji.ac.il

Received 1998 August 3; accepted 1999 July 22

ABSTRACT

Gamma-ray burst (GRB) afterglow is reasonably described by synchrotron emission from relativistic blast waves at cosmological distances. We perform detailed calculations taking into account the effect of synchrotron self-absorption. We consider emission from the whole region behind the shock front, and use the Blandford-McKee self-similar solution to describe the fluid behind the shock. We calculate the spectra and the observed image of a GRB afterglow near the self-absorption frequency, ν_a , and derive an accurate expression for ν_a . We show that the image is rather homogeneous for $\nu < \nu_a$, as opposed to the bright ring at the outer edge and the dim center, which appear at higher frequencies. We compare the spectra we obtain to radio observations of GRB 970508. We combine the calculations of the spectra near the self-absorption frequency with other parts of the spectra and obtain revised estimates for the physical parameters of the burst: $E_{52} = 0.53$, $\epsilon_e = 0.59$, $\epsilon_B = 0.014$, $n_1 = 3.0$. These estimates differ by up to 2 orders of magnitude from the estimates based on an approximate spectrum.

Subject headings: gamma rays: bursts — gamma rays: theory — radiation mechanisms: nonthermal — shock waves

1. INTRODUCTION

The detection of delayed X-ray, optical, and radio emission following a gamma-ray burst (GRB), known as GRB afterglow, is described reasonably well by emission from a spherical relativistic shell, decelerating upon collision with an ambient medium (Waxman 1997a; Wijers, Rees, & Mészáros 1997; Sari 1997; Katz & Piran 1997; Sari, Piran, & Narayan 1998). A relativistic blast wave expands through the ambient medium, continuously heating up fresh matter as it passes through the shock. In these models, the GRB afterglow is the result of synchrotron emission of the relativistic electrons of the heated matter.

Several recent works considered emission from various regions on or behind the shock front (Waxman 1997c; Sari 1998; Panaitescu & Mészáros 1998; Granot, Piran, & Sari 1999, hereafter GPS; Gruzinov & Waxman 1999). These authors considered the spectra near the peak frequency, ν_m , and found that exact calculations of the spectrum could differ by up to 1 order of magnitude from simpler estimates.

We consider emission from an adiabatic highly relativistic blast wave expanding into a cold and uniform medium. We consider the effect of the whole volume behind the shock front, the importance of which was stressed in GPS. The hydrodynamics is described by the Blandford & McKee (1976, hereafter BM) self-similar solution. Strictly speaking, this solution is valid for $\gamma \gg 1$. However, Kobayashi, Piran, & Sari (1999) have shown that it is still reasonably valid even when $\gamma \sim 2$. For typical parameters, the evolution becomes adiabatic fairly early, about 1 hr after the initial burst (Sari et al. 1999; GPS). The BM solution is valid from this time, until the evolution becomes sub-relativistic. We consider synchrotron emission and ignore Compton scattering and electron cooling. Similar to GPS, we consider several models for the evolution of the magnetic field; in this paper we also include the effects of the orientation of the magnetic field on the emission and absorption.

Synchrotron self-absorption becomes significant below a critical frequency ν_a , called the self-absorption frequency. We assume that $\nu_a \ll \nu_m$, where ν_m is the peak frequency,

which is reasonable for the first few months after the burst. While the spectrum near ν_m has been quite extensively studied, so far only order-of-magnitude estimates of the spectrum near the self-absorption frequency ν_a have been made.

For a system in which $\nu_a \ll \nu_m$, the spectrum, F_ν , is proportional to ν^2 for $\nu \ll \nu_a$, rather than the standard $\nu^{5/2}$, because almost all the low-frequency radiation is emitted by electrons with a typical synchrotron frequency much higher than ν_a (Katz 1994). The spectrum far above ν_a is proportional to $\nu^{1/3}$. In this paper we explore the spectrum near ν_a , and find how the two asymptotic forms join together. An analysis of the spectrum over a wider range of frequencies was made by Sari et al. (1999), and a detailed analysis of the spectrum near the peak frequency, fully taking into account the BM solution, was made in GPS and Gruzinov & Waxman (1999).

The physical model is described in § 2. In § 3 we describe the computational formalism. The computational formalism of some of the magnetic field models is discussed in the Appendix. The spectra and the observed image of a GRB afterglow at various frequencies for several magnetic field models are presented in § 4. In § 5 we compare the calculated spectra to radio observations of the afterglow of GRB 970508. When we use the modified calculations of the self-absorption spectrum and of the spectrum around the peak (GPS) and the cooling frequency (Sari et al. 1999), we find new estimates of the parameters of GRB 970508. These estimates are different by as much as 2 orders of magnitude from estimates based on a simpler broken power law spectrum (Wijers & Galama 1999). We also obtain constraints on the physical parameters of GRB 980329 from its radio afterglow.

2. THE PHYSICAL MODEL

The underlying model assumes an ultrarelativistic spherical blast wave expanding into a cold and uniform medium. The blast wave constantly heats fresh matter, and the observed afterglow is the result of synchrotron emission of the relativistic electrons of the heated matter. We denote

quantities measured in the local rest frame of the matter with a prime; quantities without a prime are measured in the observer frame.

We consider an adiabatic evolution, in which the fluid behind the shock is described by the BM self-similar solution. It has been numerically verified that for an adiabatic evolution with general initial conditions, the solution approaches the BM solution (Kobayashi et al. 1999). The BM solution is expressed in terms of the similarity variable, χ , which is defined by

$$\chi \equiv 1 + 16\gamma_f^2 \left(\frac{R-r}{R} \right), \quad (1)$$

where R is the radius of the shock front, r is the distance of a point from the center of the burst, and γ_f is the Lorentz factor of the matter just behind the shock. The BM solution is given by

$$\begin{aligned} n' &= 4\gamma_f n_0 \chi^{-5/4}, & \gamma &= \gamma_f \chi^{-1/2}, \\ e' &= 4n_0 m_p c^2 \gamma_f^2 \chi^{-17/12}, \end{aligned} \quad (2)$$

where n' and e' are the number density and the energy density in the local frame, respectively, γ is the Lorentz factor of the bulk motion of the matter behind the shock, m_p is the mass of a proton, and $n_0 = n_1 \times 1 \text{ cm}^{-3}$ is the proper number density of the unshocked ambient medium.

The radius of the shock front and the Lorentz factor of the matter just behind the shock on the line of sight (LOS) to the center of the burst at a given observed time, T , are given by

$$\begin{aligned} \gamma_l &= 3.65 \left(\frac{E_{52}}{n_1} \right)^{1/8} \left(\frac{T_{\text{days}}}{1+z} \right)^{-3/8}, \\ R_l &= 5.53 \times 10^{17} \left[\frac{E_{52} T_{\text{days}}}{n_1 (1+z)} \right]^{1/4} \text{ cm}, \end{aligned} \quad (3)$$

respectively, where T_{days} is the observed time in days, $E = E_{52} \times 10^{52}$ ergs is the total energy of the shell, and z is the cosmological redshift. For a given observed time T , we use the coordinates y and χ , instead of the polar coordinates r and θ , where y is defined by $y \equiv R/R_l$. R is the radius of the shock front at the time t at which a photon must be emitted in order to reach the observer at the observed time T . Since the solution is adiabatic, the Lorentz factor of the matter just behind the shock is given by $\gamma_f = \gamma_l y^{-3/2}$, and from equation (1) (Blandford & McKee 1976) we obtain

$$\gamma = \gamma_l y^{-3/2} \chi^{-1/2}. \quad (4)$$

We assume that the energy of the electrons is everywhere a constant fraction of the internal energy, $e'_e = \epsilon_e e'$, and that the shock produces a power-law electron distribution, $N(\gamma_e) = K \gamma_e^{-p}$, for $\gamma_e \geq \gamma_{\min}^{-1}$. The constants K and γ_{\min} in the electron distribution can be calculated from the number density and energy density:

$$\gamma_{\min} = \left(\frac{p-2}{p-1} \right) \frac{\epsilon_e e'}{n' m_e c^2}, \quad K = (p-1) n' \gamma_{\min}^{p-1}, \quad (5)$$

where m_e is the mass of the electron.

We consider frequencies that are much lower than the typical synchrotron frequency: $\nu \ll \nu_{\text{syn}}(\gamma_{\min}) \sim \nu_m$, where the spectral power of an electron emitting synchrotron radiation can be approximated by

$$\begin{aligned} P'_{\nu',e} &\cong \frac{2^{5/3} \pi}{\Gamma(1/3)} \frac{q_e^3 B' \sin \alpha}{m_e c^2} \left(\frac{\nu'}{\nu'_{\text{syn}}} \right)^{1/3}, \\ \nu'_{\text{syn}} &\equiv \frac{3\gamma_e^2 q_e B' \sin \alpha}{4\pi m_e c}, \end{aligned} \quad (6)$$

(Rybicki & Lightman 1979), where Γ is the gamma function, B' is the magnetic field (in the local frame), q_e is the electric charge of the electron, and α is the angle between the direction of the electron's velocity and the magnetic field, in the local frame.

Since not much is known about the origin or spacial dependence of the magnetic field, we consider three alternative models for the magnetic field: B_{eq} , B_{\perp} , and B_{rad} . B_{eq} satisfies $e'_{B'} = \epsilon_B e'$ (i.e., a constant fraction of equipartition) everywhere, where $e_B = B^2/8\pi$ is the energy density of the magnetic field. The orientation of the magnetic field in the local frame is assumed to be random in this model. This occurs when the field lines are tangled and show no preferred direction over sufficiently large volumes, which are still much smaller than the dimensions of the system. This model will be referred to as the equipartition model.

In the two remaining magnetic field models, the direction of the magnetic field in the local frame is assumed to be fixed. For the B_{rad} model it points in the radial direction, while for the B_{\perp} model it is in a random orientation within the plane perpendicular to the radial direction (in the local frame). The field strength is assumed to acquire a certain fraction of the equipartition value, $e'_{B'} = \epsilon_B e'$, on the shock front, and from then on to evolve according to the ‘‘frozen-field’’ approximation. This approximation is consistent with these two models, since for these two cases the direction of the magnetic field in the local frame stays the same, and only its magnitude evolves with time (e.g., GPS).

The consideration of alternative models for the magnetic field serves to explore the sensitivity of our results to different assumptions about the nature of the magnetic field. We find that although quantitative differences exist between the models, they are rather small. We find one qualitative difference, in the surface brightness distribution for the B_{rad} model, which is discussed in § 4.

Until very recently, there seemed to be no compelling reason to prefer one of these models over the others. However, recently Medvedev & Loeb (1999) have described a physical mechanism for the formation of a magnetic field that is adequately described by the B_{\perp} model. They suggest that a relativistic two-stream instability is capable of producing a magnetic field with $\epsilon_B \sim 10^{-5} - 10^{-1}$ that is randomly oriented in the plane of the shock front and fluctuates on scales much smaller than the scale of the emission region. Therefore, in addition to serving as a measure of the sensitivity of our results, the B_{\perp} model has the additional value of being supported by a physical model explaining the production of the magnetic field.

The shell thickness in the local frame can be estimated by R/γ , and therefore the optical depth along the LOS can be approximated by $\alpha'_{\nu'} R_l/\gamma_l$, where the absorption coefficient, $\alpha'_{\nu'}$, is taken at $y = \chi = 1$. The ‘‘back of the envelope’’ estimate for the self-absorption frequency, ν_0 , is therefore the

¹ For the energy of the electrons to remain finite, we must have $p > 2$.

frequency that satisfies $\alpha'_{\nu_0} R_l / \gamma_l = 1$. The term ν_0 is given by

$$\nu_0 = 4.24 \times 10^9 (1+z)^{-1} \left(\frac{p+2}{3p+2} \right)^{3/5} \times \frac{(p-1)^{8/5}}{p-2} \epsilon_e^{-1} \epsilon_B^{1/5} E_{52}^{1/5} n_1^{3/5} \text{ Hz} . \quad (7)$$

We also define a ‘‘standard’’ flux density, F_0 , that is an approximate expression for the flux density at the self-absorption frequency. The peak flux and peak frequency can be approximated by

$$F_{\nu_m} \equiv \frac{(1+z)}{3} \frac{n_1 R_l^3}{d_L^2} \left(\frac{\gamma P'_e}{\nu'_{\text{syn}}} \right) \quad (y = \chi = 1) ,$$

$$\nu_m \equiv \nu_{\text{syn}}(\gamma_{\text{min}}, y = \chi = 1) \quad (8)$$

(see F_0 and ν_T in GPS), where $P'_e = (4/3)\sigma_T c \gamma_e^2 e'_B$ is the total emitted power of an extreme relativistic electron (Rybicki & Lightman 1979), σ_T is the Thomson cross section, and d_L is the luminosity distance.² Now we can define $F_0 \equiv F_{\nu_m}(\nu_0/\nu_m)^{1/3}$,

$$F_0 = 1.31 \sqrt{1+z} \left(\frac{p+2}{3p+2} \right)^{1/5} \frac{(p-1)^{6/5}}{p-2} \times \left(\frac{d_L}{10^{28} \text{ cm}} \right)^{-2} \epsilon_e^{-1} \epsilon_B^{2/5} E_{52}^{9/10} n_1^{7/10} T_{\text{days}}^{1/2} \text{ mJy} . \quad (9)$$

We express the observed frequency, ν , in units of ν_0 , $\nu \equiv \phi \nu_0$, thus introducing the dimensionless variable ϕ , which we use to express our results.

The hydrodynamic evolution becomes adiabatic after

$$T_0 = 0.02 \times (1+z) \left(\frac{\epsilon_B}{0.1} \right)^2 \left(\frac{\epsilon_e}{0.1} \right)^2 E_{52} n_1 \text{ days} . \quad (10)$$

(Sari et al. 1999). At this stage, the typical electron (on the LOS, with $\gamma = \gamma_{\text{min}}$), which radiates around ν_m , cools on the dynamical time of the system (i.e., the time required for a significant expansion of the fireball). The cooling frequency, ν_c , at a given time is the synchrotron frequency of an electron that cools during the dynamical time. T_0 is defined as the time at which $\nu_c = \nu_m$, i.e., the time at which the typical electron cools at the dynamical time of the system. The ratio between the cooling time of the typical electron and the dynamical time scales as $T^{1/2}$ (Waxman 1997b). Therefore, for $T > T_0$ a typical electron cools on a timescale larger than the dynamical time of the system, implying an adiabatic evolution, which is described by the BM solution.

Various estimates of the burst parameters yield $E_{52} \sim n_1 \sim 1$ and $\epsilon_e \epsilon_B \sim 0.01$ (Wijers & Galama 1999; GPS; Waxman 1997b). For these values, $T_0 \sim 1$ hr. For the values of the physical parameters of GRB 970508, which we calculate later, we obtain $T_0 = 3.4 \times 10^3 \text{ s} \approx 1$ hr. Thus, at the time of the radio afterglow of this burst, around 1 week after the burst, the hydrodynamic evolution should be well within the adiabatic regime.

3. THE FORMALISM

We consider a system that is moving relativistically while emitting radiation, and obtain a formula for the flux density

² Here and following later we use a general cosmological model. For a given model, we should substitute the appropriate expression for $d_L(1+z, H_0)$.

measured by a distant observer, allowing for self-absorption.

The specific intensity, I_ν (energy per unit time per unit area per unit frequency per unit solid angle), satisfies the radiative transfer equation

$$\frac{dI_\nu}{ds} = j_\nu - \alpha_\nu I_\nu , \quad (11)$$

where j_ν and α_ν are the emission coefficient and the absorption coefficient, respectively, and s is the distance along the beam. When self-absorption becomes important, the contribution to I_ν depends on the optical depth along the path within the emitting system, and I_ν should be integrated separately for every trajectory.

A photon emitted at a location (r, θ) at a time t in the observer frame reaches the observer at an observed time T , given by

$$\frac{T}{1+z} = t - \frac{r\mu}{c} , \quad (12)$$

where $\mu \equiv \cos \theta$ (for more details on the coordinates, see GPS).

Since the observer is distant, the trajectory of a photon that reaches the observer is almost parallel to the LOS in the observer frame (see Fig. 1). We can therefore parameterize the various trajectories by their distance from the LOS. The distance R_\perp of a point from the LOS is given by

$$R_\perp \equiv r \sin \theta \cong R_l y \sqrt{1 - \mu^2} \cong \frac{\sqrt{2} R_l}{4\gamma_l} \sqrt{y - \chi y^5} . \quad (13)$$

The maximal value of R_\perp is obtained for $\chi = 1$, $y = 5^{-1/4}$, and is given by

$$R_{\perp, \text{max}} = 3.91 \times 10^{16} \left(\frac{E_{52}}{n_1} \right)^{1/8} \left(\frac{T_{\text{days}}}{1+z} \right)^{5/8} \text{ cm} . \quad (14)$$

This is the observed size of the fireball. The size of the fireball was estimated for GRB 970508 from its radio afterglow in two independent ways, using scintillation (Frail et al. 1997) and using absorption (Frail et al. 1997; Katz & Piran 1997), and was found to be $R_{\perp, \text{max}} \approx 10^{17} \text{ cm}$ about 1 month after the burst. Substituting the values we obtain for

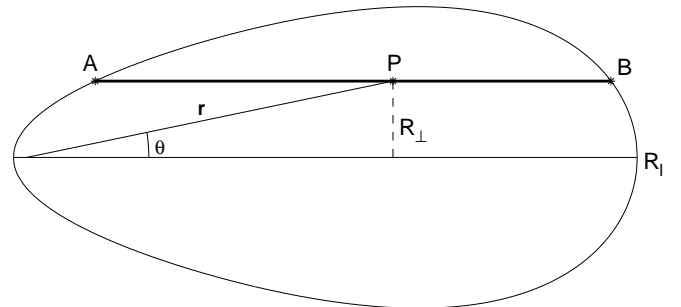


FIG. 1.—Egg-shaped curve showing the boundary of the region from which photons reach a distant observer simultaneously. The observer is located far to the right, and the symmetry axis is the LOS from the source of the burst to the observer. The bold line represents the trajectory of a photon that reaches the observer. For a distant observer, these trajectories are almost parallel to the LOS, and are therefore characterized by their distance R_\perp from the LOS. $I_\nu = 0$ at point A, and reaches its final value at point B. A photon emitted at a point P can be absorbed or cause stimulated emission at any point along the trajectory, until it passes the shock front at point B.

TABLE 1

ESTIMATES OF THE PHYSICAL PARAMETERS OF GRB 970508

Model (1)	Broken	Modified v_a (3)	Modified v_a ,
	Power Law (2)		v_m, F_{v_m}, v_c (4)
E_{52}	3.5	1.6	0.53
ϵ_e	0.12	0.26	0.59
ϵ_B	0.089	0.017	0.014
n_1	0.030	0.51	3.0

NOTE.—Col. (2) depicts the values of the physical parameters of GRB 970508 as calculated by Wijers & Galama 1999. Cols. (3) and (4) show how these values change when some of the equations they used in the calculation are corrected. Col. (1) lists the measurable quantities whose equations were altered.

the physical parameters of this burst (Table 1, col. [4]) into equation (14) and using $z = 0.835$, we obtain $R_{\perp, \max} = 1.6 \times 10^{17}$ cm, 25 days after the burst. Our value for $R_{\perp, \max}$ corresponds to an angular size of

$$\theta_{\text{obs}} = R_{\perp, \max}/d_A = 8.2 \mu\text{as} \quad (15)$$

for $\Omega = 1$, $\Lambda = 0$, and $H_0 = 65 \text{ km s}^{-1} \text{ Mpc}^{-1}$, where $d_A = d_L/(1+z)^2$ is the angular distance to the burst. This is somewhat larger than the value estimated by Frail et al. (1997), $\theta_{\text{obs}} \approx 3 \mu\text{as}$. However, we believe that the results are consistent in view of the large uncertainties of the scintillation estimates.

We express R_{\perp} in units of $R_{\perp, \max}$, introducing the dimensionless variable

$$x \equiv \frac{R_{\perp}}{R_{\perp, \max}} = \frac{5^{5/8}}{2} \sqrt{y - \chi y^5}. \quad (16)$$

In order to solve equation (11), explicit expressions for the absorption and the emission coefficients are needed. We consider an isotropic electron velocity distribution for all the magnetic field models. In the rest of this section we address the equipartition model, B_{eq} . A similar derivation for the B_{rad} and B_{\perp} models is given in the Appendix.

The electron velocity is isotropic and the magnetic field is randomly oriented in the B_{eq} model, and therefore the local emissivity is isotropic in this case. Since $P'_{\nu', e} \propto \sin^{2/3} \alpha$, we can use the average value of $\sin^{2/3} \alpha$ over all solid angles, $\langle \sin^{2/3} \alpha \rangle_{\Omega} = \sqrt{\pi} \Gamma(1/3)/5\Gamma(5/6)$. The total spectral power per unit volume in the local frame is given by

$$P'_{\nu'} = \int_{\gamma_{\min}}^{\infty} d\gamma_e N(\gamma_e) P'_{\nu', e} \\ = \frac{64\pi^{13/6} 3^{2/3}}{5\Gamma(5/6)} \frac{(p-1)^{5/3}}{(3p-1)(p-2)^{2/3}} \frac{\epsilon_B^{1/3} \gamma_l n_0^{4/3} q_e^{8/3} v^{1/3}}{m_p^{1/3} c y^{3/2} \chi^{29/18}}. \quad (17)$$

Since the emission and absorption are isotropic in the local rest frame of the matter, $j'_{\nu'} = P'_{\nu', e}/4\pi$, and the absorption coefficient is given by

$$\alpha'_{\nu'} = \frac{(p+2)}{8\pi m_e v'^2} \int_{\gamma_{\min}}^{\infty} d\gamma_e P'_{\nu', e}(\gamma_e) \frac{N(\gamma_e)}{\gamma_e} \\ = \frac{8\pi^{7/6} 3^{2/3}}{5\Gamma(5/6)} \frac{(p+2)(p-1)^{8/3}}{(3p+2)(p-2)^{5/3}} \frac{\epsilon_B^{1/3} n_0^{4/3} q_e^{8/3}}{\epsilon_e^{5/3} m_p^{4/3} c v'^{5/3} \chi^{13/9}} \quad (18)$$

(Rybicki & Lightman 1979). Keeping in mind that j_{ν}/v^2 and α_{ν} are Lorentz invariant and $v' = v\gamma(1 - \beta\mu)$, we can write

the radiative transfer equation (eq. [11]) explicitly. We first write an expression for the optical depth to the observer, which will later help us gain some intuition for the results. The optical depth to the observer is given by

$$\tau(x, y) = \int \alpha_{\nu} ds \\ = \frac{2}{\phi^{5/3}} \int_y^{y_{\max}(x)} dy \frac{y^{5/3}}{\chi^{10/9}(x, y)[1 + 7\chi(x, y)y^4]^{2/3}}, \quad (19)$$

where $\chi(x, y)$ is obtained from equation (16), $y_{\max}(x)$ is obtained by solving $\chi(x, y) = 1$ for y , and $\phi \equiv v/v_0$.

We define a ‘‘typical’’ specific intensity, I_0 , by $I_0 \equiv S_{\nu}(y = \chi = 1)$, where the source function S_{ν} is defined as $S_{\nu} \equiv j_{\nu}/\alpha_{\nu}$. Expressing I_{ν} in units of I_0 , $I_{\nu} \equiv \tilde{I}_{\nu} I_0$, we write equation (11) in terms of the dimensionless variables \tilde{I}_{ν} ,

$$\frac{d\tilde{I}_{\nu}}{dy} = \frac{2y^{5/3}}{\phi^{5/3} \chi^{10/9}(1 + 7\chi y^4)^{2/3}} \left[\frac{8y\chi^{1/3}}{(1 + 7\chi y^4)} - \tilde{I}_{\nu} \right], \quad (20)$$

where we used $ds \cong R_l dy$. This equation can be solved numerically for a given magnetic field model and a given value of ϕ for different values of x , thus obtaining $I_{\nu}(x)$.

Regardless of the magnetic field model, the observed flux density is given by

$$F_{\nu}(T) \cong \frac{(1+z)}{d_L^2} \int dS_{\perp} I_{\nu} \\ = 2\pi(1+z) \left[\frac{R_{\perp, \max}(T)}{d_L} \right]^2 \int_0^1 x dx I_{\nu}(x, T). \quad (21)$$

As can be seen from equation (21), the surface brightness is proportional to I_{ν} : $dF_{\nu}/dS_{\perp} \propto I_{\nu}$. This means that we also obtain the observed image of a GRB afterglow by calculating the observed flux density in this way.

4. THE SPECTRA AND OBSERVED IMAGE

Solving equations (20), (A15), and (A16), we obtain I_{ν} for the three magnetic field models B_{eq} , B_{rad} , and B_{\perp} , respectively. The spectra for these models are then obtained using equation (21), and are shown in Figure 2. We define the self-absorption frequency, ν_a , as the frequency at which the asymptotic high- and low-frequency power laws meet. For the equipartition magnetic field model, B_{eq} , we obtain

$$\nu_a = 0.247 \times \nu_0, \quad (22)$$

while for the B_{\perp} model it is lower by 1.3%, and for the B_{rad} model it is higher by 2.0%. For $\nu \ll \nu_a$ the system is optically thick, and therefore the radiation reaching an observer is emitted essentially near the edge of the system that faces the observer. It reflects the electron distribution there, and it is independent of the magnetic field model (as we show explicitly in the Appendix). For $\nu > \nu_a$ the system is optically thin, and the flux density is different for the various magnetic field models, although the difference is small.

The ratio τ/τ_{\max} (where τ is the optical depth and τ_{\max} is its maximal value) for the equipartition model, B_{eq} , is shown in Figure 3. Since $\tau_{\nu} \propto \phi^{-5/3}$ everywhere, τ/τ_{\max} is independent of frequency. The contour lines of τ_{ν} are dense where the absorption coefficient α_{ν} is large. The term τ_{\max} is obtained at $x \cong 0.93$, i.e., quite close to the edge of the image, since then the whole trajectory to the observer is relatively close to the shock front, implying large values of α_{ν} and a large contribution to τ_{ν} . The value of τ_{\max} is a good

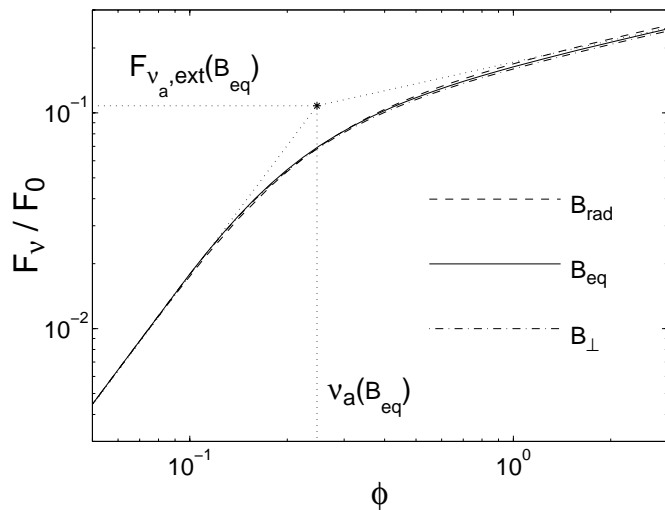


FIG. 2.—Spectra for different magnetic field models. The frequency, ν_a , and the flux density, $F_{\nu_a, \text{ext}}$, are defined at the point at which the extrapolations of the power laws meet, as illustrated for the equipartition magnetic field model B_{eq} . The term ν_a is constant in time, while $F_{\nu_a, \text{ext}} \propto T^{1/2}$, and both hardly change between the different magnetic field models. For $\phi \ll 1$ ($\nu \ll \nu_a$) the system is optically thick, and the flux density reflects the electron distribution (or the Lorentz-boosted “effective temperature” of the electrons) and is independent of the magnetic field model.

indicator for the opacity of the system, and for the equipartition model, B_{eq} , it is given by $\tau_{\text{max}} = 1.08(\nu/\nu_a)^{-5/3}$.

We define $F_{\nu_a, \text{ext}}$ as the extrapolated flux density at ν_a (see Fig. 2). For the equipartition model, B_{eq} , we obtain

$$F_{\nu_a, \text{ext}} = 0.108F_0, \quad (23)$$

while for the B_{\perp} model it is lower by 2.6%, and for the B_{rad} model it is higher by 4.1%. The actual flux density at ν_a is around 35% lower than $F_{\nu_a, \text{ext}}$: $F_{\nu_a} \cong 0.65F_{\nu_a, \text{ext}}$. The values of $F_{\nu_a, \text{ext}}$ and ν_a are useful, since for $\nu \ll \nu_a$ (assuming $\nu_m > \nu_a$), the flux density is given by $F_{\nu} \cong F_{\nu_a, \text{ext}}(\nu/\nu_a)^2$, and for $\nu_a \ll \nu \ll \nu_m$ it is given by $F_{\nu} \cong F_{\nu_a, \text{ext}}(\nu/\nu_a)^{1/3}$. Both approx-

imations are already good within a few percent for frequencies a factor of ~ 3 below or above ν_a , respectively.

It is interesting to compare the spectrum obtained for the BM solution to that obtained for a simplistic model of a static homogeneous disk. This comparison should help us learn whether the fact that the spectrum is rounded up near ν_a should be attributed mainly to the specific hydrodynamics used, or whether it is a more general feature of a calculation accounting for self-absorption. For a static disk we obtain the well-known result

$$F_{\nu} = F_{\nu_a, \text{ext}}^* \psi^2 (1 - \exp[-\psi^{-5/3}]), \quad \psi \equiv \frac{\nu}{\nu_a^*}, \quad (24)$$

where the constants $F_{\nu_a, \text{ext}}^*$ and ν_a^* are determined by the radius and width of the disk and by the hydrodynamic parameters of the emitting matter within the disk. If these parameters are set so that the two starred quantities equal those in equations (23) and (22), respectively, the resulting flux density is very similar to that obtained for the BM solution. Substituting equations (23) and (22) into equation (24) can thus serve as a good approximation (better than 3% for all three magnetic field models) for the observed flux density at $\nu \ll \nu_m$. This similarity implies that the shape of the spectrum near ν_a is rather independent of the specific hydrodynamic solution considered. On the other hand, the exact values of ν_a and $F_{\nu_a, \text{ext}}$ depend significantly on the hydrodynamics, and cannot be determined without the detailed calculation. A simplified calculation for ν_a^* could, for example, yield ν_0 (eq. [7]) instead of ν_a , which is given in equation (22).

The surface brightness as a function of $x \equiv R_{\perp}/R_{\perp, \text{max}}$ for the equipartition magnetic field model, B_{eq} , is shown in Figure 4 for a few representative values of $\phi \equiv \nu/\nu_0$. An illustration of the observed image of a GRB afterglow, which is implied from the surface brightness, is shown in Figure 5 for B_{eq} . As a reference, the image for $\nu \gg \nu_m$, which was derived in GPS, is also presented.

For $\nu \gg \nu_a$ the system is optically thin, and the result coincides with that obtained in GPS for $\nu \ll \nu_m$. There is a bright ring near the outer edge of the image, and the surface

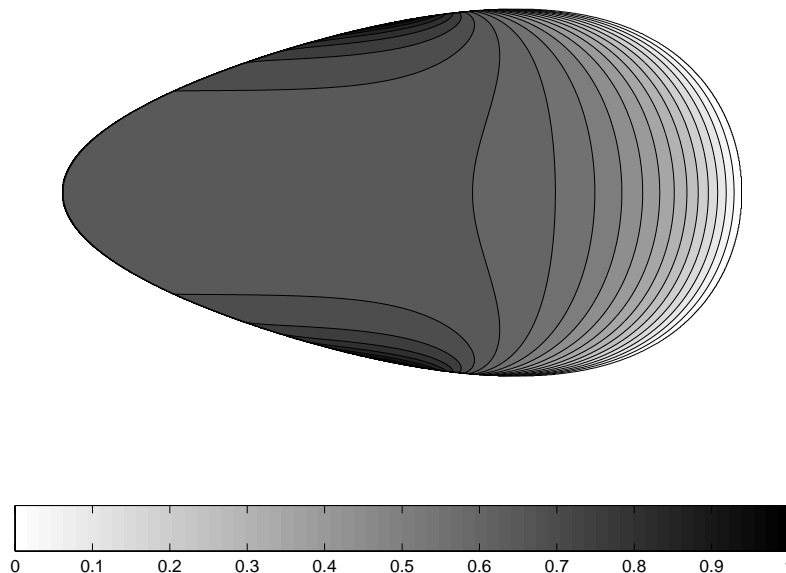


FIG. 3.—Optical depth τ to the observer, divided by the maximal optical depth [$\tau = \tau_{\text{max}} = 1.08 \times (\nu/\nu_a)^{-5/3}$ is black], for B_{eq} . The value of τ_{max} is obtained at $x \equiv R_{\perp}/R_{\perp, \text{max}} = 0.93$. The contour lines are equally spaced, with a 5% interval between following contour lines.

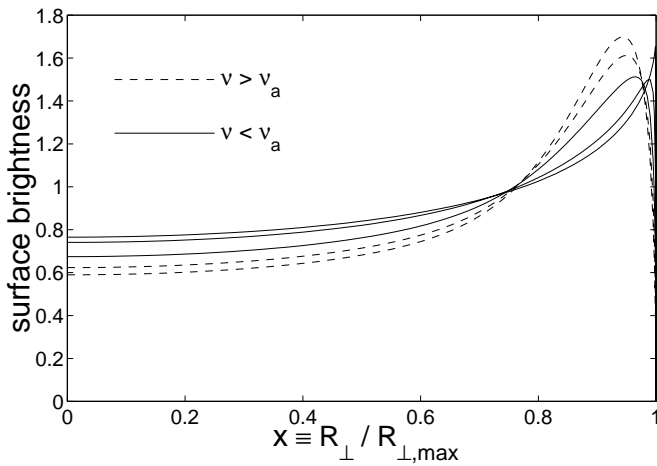


FIG. 4.—Surface brightness as a function of x , divided by the average surface brightness, for the B_{eq} model, for $\log_{10}(\phi) = -1.5, -1-0.75, -0.5$, and 0 (corresponding to $\nu/\nu_a = 0.13, 0.40, 0.72, 1.28$, and 4.05 , respectively). At high frequencies, the contrast between the center and the edge of the image is larger than at low frequencies. At low frequencies the system is optically thick, and the surface brightness reflects the “effective temperature” of the electrons at the edge of the “egg” depicted in Fig. 1, on the side facing the observer.

brightness at the center of the image is 58% of its average value. As ν decreases, the contrast between the edge and the center of the image decreases, and the system becomes increasingly optically thick. As a result, the surface brightness reflects the Lorentz-boosted “effective temperature” of

the electron distribution, at the outer edge of the “egg” depicted in Figures 1 and 3, on the side facing the observer. Larger values of x correspond to smaller shock radii, R , and since the electrons possess a larger Lorentz factor (i.e., a larger “effective temperature”) at smaller radii, the surface brightness increases with x . This is true as long as the optical depth is still large. Since the length of the trajectory within the system approaches zero as $x \rightarrow 1$, for every given frequency ν , the system becomes optically thin for values of x sufficiently close to 1. For frequencies smaller than ν_a by more than 1 or 2 orders of magnitude, this occurs at $1 - x \ll 1$, so that the drop in the surface brightness near $x = 1$ is extremely sharp. For $\nu \ll \nu_a$, the surface brightness at the center of the image is 77% of its average value, resulting in an almost uniform disk, rather than the ring obtained for $\nu > \nu_a$. The uniformity of the image for $\nu \ll \nu_a$ stands out even more when compared to $\nu \gg \nu_m$, where there is a thin bright ring on the outer edge of the image, and the surface brightness at the center is only a few percent of its maximal value.

Figure 6 shows the surface brightness as a function of x for the B_{rad} model, for several representative values of ϕ . Figure 7 depicts the surface brightness as a function of x for frequencies in the range $\nu_a \ll \nu \ll \nu_m$ for all three magnetic field models. The surface brightness distribution for the B_{\perp} model is quite similar to that of the B_{eq} model, and is slightly more homogeneous in the optically thin regime. On the other hand, the surface brightness distribution for the B_{rad} model is quite different from that of the other two models,

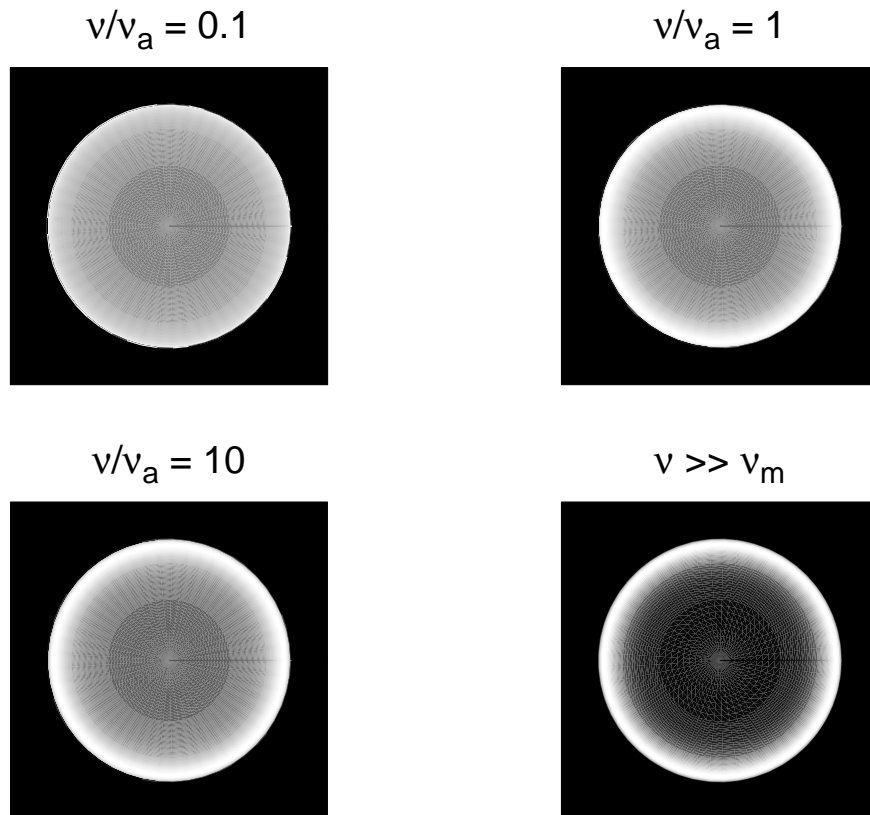


FIG. 5.—Observed image of a GRB afterglow, at several frequencies, for the B_{eq} model. At high frequencies there is a bright ring near the outer edge of the image, and the contrast between the center and the edge of the image is larger than at low frequencies. At low frequencies the surface brightness increases as one moves from the center toward the edge, until it drops very sharply, due to the fact that the system becomes optically thin near the edge. The last image, for $\nu \gg \nu_m$, is taken from GPS. It was calculated for $p = 2.5$ and is provided as a reference, to illustrate the change in the relative surface brightness along the image over a large range of frequencies. At $\nu \gg \nu_m$ there is a thin bright ring at the outer edge of the image, and the surface brightness at the center is only a few percent of its maximal value.

since the surface brightness vanishes at the center of the image ($x = 0$). This is due to the fact that for $x = 0$, on the LOS, the magnetic field points at the observer, and the synchrotron emission vanishes in the direction of the magnetic field. The absorption coefficient, and therefore the optical depth, also vanish on the LOS (see Fig. 8). Surface brightness vanishes for $x = 0$, also in the optically thick regime. However, since for any $x > 0$ the system becomes optically thick at sufficiently low frequencies, all three models have the same SB distribution for $\nu \ll \nu_a$. This was to be expected, since $I_\nu = S_\nu$ in this regime, and we show in the Appendix that S_ν is independent of the model for the magnetic field.

The large difference in the surface brightness distribution for $\nu_a \ll \nu \ll \nu_m$ between the B_{rad} model and the other

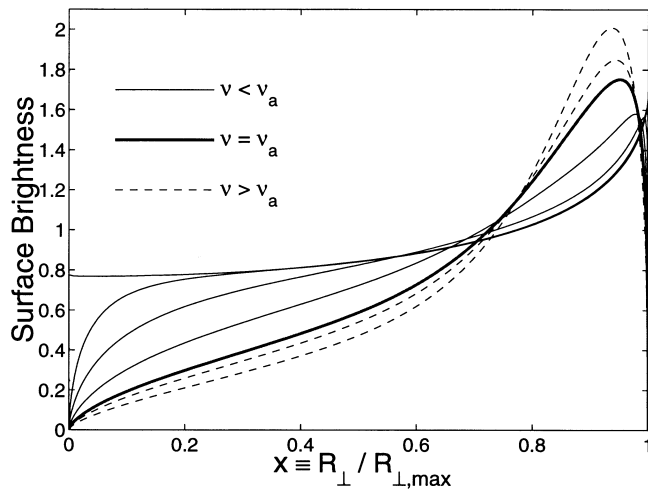


FIG. 6.—Surface brightness as a function of x , divided by the average surface brightness, for the B_{rad} model. The various traces correspond to $\nu/\nu_a = 0.22, 0.35, 0.56, 1$, and to the limits $\nu \ll \nu_a$ and $\nu_a \ll \nu \ll \nu_m$. The surface brightness vanishes at the center of the image ($x = 0$), and the contrast between the center and the edge of the image is significantly larger than for the other magnetic field models. As ν decreases below ν_a the system becomes increasingly optically thick, and the surface brightness approaches the same value as for the other magnetic field models.

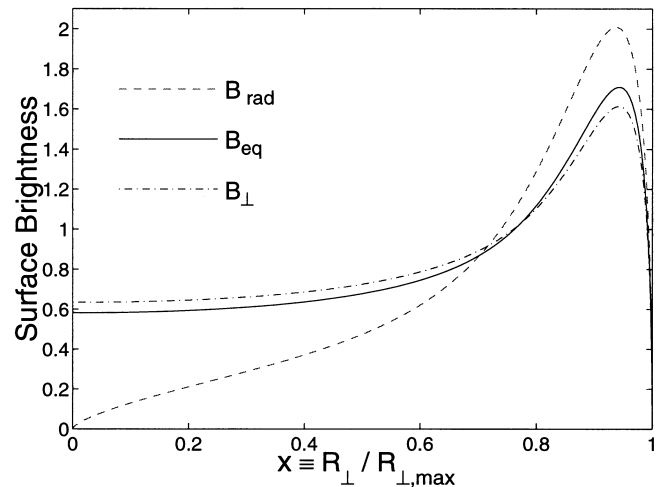


FIG. 7.—Surface brightness as a function of x , divided by the average surface brightness, for $\nu_a \ll \nu \ll \nu_m$. The different curves are for the different magnetic field models. While B_{eq} and B_{\perp} show a similar surface brightness distribution, the surface brightness for B_{rad} is qualitatively different, since it vanishes at the center of the image ($x = 0$).

models could be useful if a radio image of a GRB afterglow is resolved in the optically thin regime. In this case, we might learn something about the magnetic field orientation within the shocked matter.

5. COMPARISON TO OBSERVATIONS

We now fit the theoretical spectra we have calculated to the radio frequencies observations of the afterglow of GRB 970508 (Fig. 4 of Shepherd et al. 1998). It is hoped that a future near enough GRB will result in a sufficient resolution that we will be able to compare the predicted images of a GRB afterglow to observations.

The radio observations were made about 1 week after the burst ($T_{\text{days}} \approx 7$). The evolution of GRB 970805 is expected to be still relativistic at this stage. Since we expect the evolution of this burst to become adiabatic after 1 hr or so (Sari et al. 1998; GPS), our analysis should be applicable here.

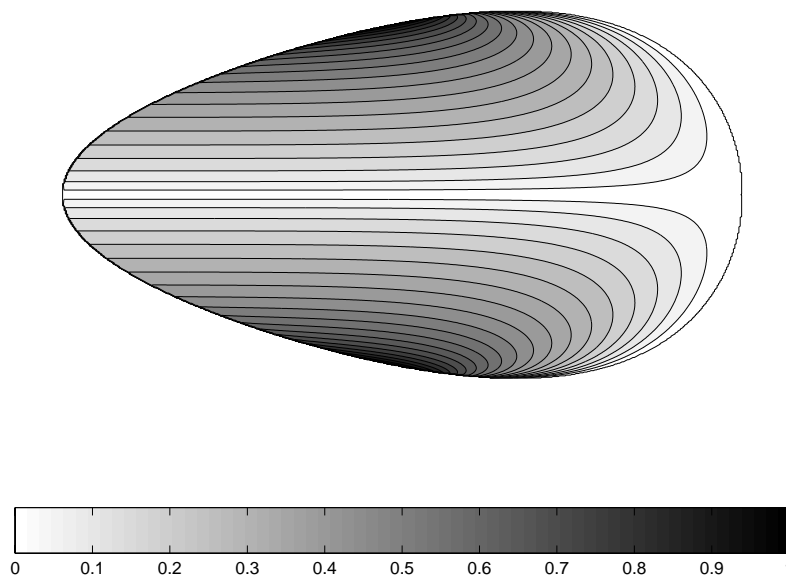


FIG. 8.—Optical depth to the observer, τ , divided by the maximal optical depth [$\tau = \tau_{\text{max}} = 1.25 \times (\nu/\nu_a)^{-5/3}$ is black], for the B_{rad} model. The value of τ_{max} is obtained at $x \equiv R_{\perp}/R_{\perp,\text{max}} = 0.92$. The contour lines are equally spaced, with a 5% interval between following contour lines. The absorption coefficient vanishes along the LOS, causing the optical depth to do the same.

Since both ν_0 and F_0 depend on the parameters of the model (see eqs. [7] and [9]), we have 2 degrees of freedom in trying to fit the calculated spectra to the observed data. We fit the equipartition magnetic field model, B_{eq} , to the data of Shepherd et al. (1998) and obtain

$$\begin{aligned} \nu_a &= 3.1 \pm 0.4 \times 10^9 \text{ Hz} , \\ F_{\nu_a, \text{ext}} &= 450 \pm 37 \text{ } \mu\text{Jy} , \end{aligned} \quad (25)$$

with $\chi^2/\text{dof} = 0.48$. The fit is presented in Figure 9.

The errors quoted are statistical errors. The actual errors are probably larger, due to uncertainty in the radio flux due to scintillation, and due to the fact that not all the observations are exactly simultaneous (see Shepherd et al. 1998).

Substituting these results in equations (22) and (23), respectively, we obtain two constraints on the physical parameters of the burst. The luminosity distance depends on the cosmological model. For $\Omega = 1$, $\Lambda = 0$ (which implies $d_L = 2[1 + z - (1 + z)^{1/2}]c/H_0$), $H_0 = 65 \text{ km s}^{-1} \text{ Mpc}^{-1}$, and $z = 0.835$, we find

$$\frac{(p-1)^{8/5}}{p-2} \left(\frac{p+2}{3p+2} \right)^{3/5} \epsilon_e^{-1} \epsilon_B^{1/5} E_{52}^{1/5} n_1^{3/5} = 5.42 , \quad (26)$$

$$\frac{(p-1)^{6/5}}{p-2} \left(\frac{p+2}{3p+2} \right)^{1/5} \epsilon_e^{-1} \epsilon_B^{2/5} E_{52}^{9/10} n_1^{7/10} = 1.65 . \quad (27)$$

Equation (26), which arises from substituting the value of ν_a extracted from the data (eq. [25]) into equation (22), is different by a factor of ~ 2 from equation (22) of Wijers & Galama (1999). The difference is mainly due to a different theoretical value they used for ν_a . They also used a slightly different value of ν_a as corresponding to the same observational data. This factor of ~ 2 implies significant corrections to the values of the physical parameters of the burst (see Table 1, col [3]). For example, n_1 (or n in their notation) becomes a factor of ~ 17 larger: $n_1 = 0.51$ instead of $n_1 = 0.030$.

We modify the estimates further using more detailed calculations of the spectrum near the peak flux (GPS) and a different estimate for the cooling frequency, ν_c (Sari et al. 1998). We discover that the values obtained for the physical parameters of a burst are very sensitive to the theoretical model of the spectrum. In order to illustrate this, we show in

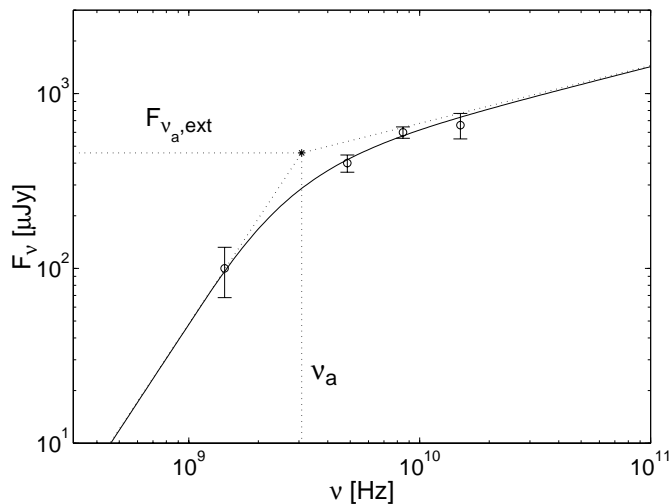


FIG. 9.—Fit of the calculated spectra to radio observations of the afterglow of GRB 970508 made approximately 1 week after the burst. We obtained $\nu_a = 3.1 \pm 0.4 \times 10^9 \text{ Hz}$ and $F_{\nu_a, \text{ext}} = 450 \pm 37 \text{ } \mu\text{Jy}$.

Table 1 the physical parameters of GRB 970508 for different estimates of the spectrum. Column (2) uses a broken power law spectrum (Wijers & Galama 1999); column (3) uses a corrected theoretical value for ν_a from equation (22) and a corrected observational value for ν_a from equation (25); and column (4) adds modified theoretical values to ν_m and F_{ν_m} (which are taken from GPS, denoted there as ν_{peak} and $F_{\nu, \text{max}}$) and a different estimate for the cooling frequency ν_c (from Sari et al. 1998), keeping the observational values from Wijers & Galama (1999).

Our best values (with all modifications added) are $E_{52} = 0.53$, $\epsilon_e = 0.59$, $\epsilon_B = 0.014$, and $n_1 = 3.0$. These values differ by up to 2 orders of magnitude from the values obtained by Wijers & Galama (1999) using a broken power law spectra. One must keep in mind that it is difficult to obtain an accurate estimate of the various observables from the observed data. It is especially difficult to determine ν_m , F_{ν_m} , and ν_c . Therefore, beyond obtaining a better estimate of the physical parameters of the burst, these calculations also show the sensitivity of this method and the need for more accurate data.

Using these values of the parameters (from col. [4] of Table 1), we can determine the physical conditions at the time of the comparison. We find that

$$\gamma \cong 1.8y^{-3/2}\chi^{-1/2} , \quad R \cong 5.0 \times 10^{17} y \text{ cm} ,$$

$$\gamma_{\text{min}} \cong 640y^{-3/2}\chi^{-1/6} , \quad B'_{\text{eq}} \cong 0.14y^{-3/2}\chi^{-17/24} \text{ G} . \quad (28)$$

Brainerd (1997, 1998) has obtained a lower limit on the energy of a relativistic electron distribution emitting self-absorbed synchrotron radiation, using the value of the observed flux density and the angular size of the system. His limit is very sensitive to the angular size of the source at the time of the observation. Specifically, for GRB 970508, the observed angle of the source 25 days after the burst is $2\theta_{\text{obs}} \equiv 2R_{\perp, \text{max}}/d_A = 16.4 \text{ } \mu\text{s}$ (eq. 15), where Brainerd uses the observed diameter of the fireball rather than its observed radius when defining the observed angle. Using this value, the Brainerd lower limit for the energy stored in electrons in the observer frame for a spherical shell is $\sim 10^{48}$ ergs. From Table 1 we see that the energy in electrons, $\epsilon_e E$, is a few $\times 10^{51}$ ergs, which is consistent with his limit. On the other hand, the value we have calculated for the observed size of the fireball falls somewhat outside the allowed volume in parameter space, according to Brainerd's calculations. Since both estimates are based on the same physical idea, while here we perform a more detailed analysis, we expect that this minor discrepancy is due to the approximate nature of Brainerd's treatment.

Sufficient observational data has been gathered on the radio afterglow of GRB 980329 to enable a fit similar to the one we made for GRB 970508. Such a fit was carried out by Taylor et al. (1998). The theoretical formula for the flux density that was used for the fit is identical to equation (24). Since this is a good approximation for the shape of the spectrum near ν_a , we can use the values extracted from the data to obtain constraints on the physical parameters of GRB 980329.

The values used by Taylor et al. (1998) for the flux density are mean values over the first month. Since $F_{\nu_a} \propto T^{1/2}$, this corresponds to the flux density at $T_{\text{days}} \sim 15$. The values extracted from the data are

$$\nu_a \cong 1.3 \times 10^{10} \text{ Hz} , \quad F_{\nu_a, \text{ext}} \cong 600 \text{ } \mu\text{Jy} . \quad (29)$$

Substituting these results in equations (22) and (23), respectively, we obtain two constraints on the parameters of GRB 980329. For $\Omega = 1$, $\Lambda = 0$, and $H_0 = 65 \text{ km s}^{-1} \text{ Mpc}^{-1}$, we find

$$(1+z)^{-1} \frac{(p-1)^{8/5}}{p-2} \left(\frac{p+2}{3p+2} \right)^{3/5} \epsilon_e^{-1} \epsilon_B^{1/5} E_{52}^{1/5} n_1^{3/5} \cong 12.4, \quad (30)$$

$$\frac{\sqrt{1+z}}{(1+z - \sqrt{1+z})^2} \frac{(p-1)^{6/5}}{p-2} \left(\frac{p+2}{3p+2} \right)^{1/5} \times \epsilon_e^{-1} \epsilon_B^{2/5} E_{52}^{9/10} n_1^{7/10} \cong 8.86, \quad (31)$$

where the redshift, z , of this burst is not known.

6. DISCUSSION

We have considered synchrotron emission from a system moving relativistically, taking into account the effect of synchrotron self-absorption. We have assumed an adiabatic evolution and used the self-similar solution of Blandford & McKee (1976) to describe the matter behind the shock. This solution describes an extreme relativistic spherical blast wave expanding into a cold uniform medium. Our calculations accounted for the emission from the whole region behind the shock front.

We have assumed a power-law distribution of electrons with an isotropic velocity distribution. Three alternative models have been considered for the evolution of the magnetic field: an equipartition model with a randomly oriented field, B_{eq} , and two models in which the field points either at the radial or tangential directions, B_{rad} and B_{\perp} , respectively. We have calculated the flux density at frequencies near the self-absorption frequency, ν_a , under the assumption that $\nu_a \ll \nu_m$.

We have obtained an expression for the self-absorption frequency, ν_a , which we define as the frequency at the point at which the extrapolations of the asymptotic power laws above and below the ν_a meet. The value we obtained for ν_a is close to the value obtained by Wijers & Galama (1999), and larger than the value obtained by Waxman (1997b) by a factor of ~ 4 for $p = 2.5$ (or a factor of ~ 7 for $p = 2.2$). It also shows very little dependence on the magnetic field model.

We have calculated the observed spectra near ν_a for three different magnetic field models (Fig. 4). The spectrum differs by more than a few percent from the asymptotic power laws only for frequencies less than half an order of magnitude above or below ν_a . This applies to all the magnetic field models we have considered.

Together with the afterglow images obtained in GPS, we now have a complete set of the observed image for the equipartition B_{eq} model over a wide range of frequencies (see Figs. 4 and 5). For $\nu \gg \nu_m$ there is a thin bright ring on the outer edge of the image, and the surface brightness at the center of the image is only a few percent of its maximal

value. For $\nu_a \ll \nu \ll \nu_m$ there is a wider ring, and the contrast between the center and the edge of the image is smaller, with 58% of the average surface brightness at the center. For $\nu \ll \nu_a$ the image is even more homogeneous, with 77% of the average surface brightness at the center.

The observed image for the B_{\perp} model is quite similar to that of B_{eq} . For B_{rad} , on the other hand, the surface brightness vanishes at the center of the image, since synchrotron emission vanishes in the direction of the magnetic field (see Figs. 6 and 7).

The observed image in the radio frequencies is of special importance, since the best resolution is obtained in radio, with VLBI. A sufficient resolution could be reached with a nearby GRB ($z \sim 0.2$) to resolve the inner structure of the image in radio frequencies. In this case, the qualitative difference in the observed image between the different magnetic field models might serve to explore the nature of the magnetic field at the source. This may also serve to test models for the generation of the magnetic field, such as that of Medvedev & Loeb (1999), according to which the magnetic field that is generated is consistent with our B_{\perp} model.

We have fitted the theoretical spectra to observational data of the afterglow of GRB 970508 (Shepherd et al. 1998) and extracted the values of ν_a and $F_{\nu_a, \text{ext}}$ from the data (eq. 25). Substituting these values into the theoretical expressions, we obtained two equations for the physical parameters. The behavior of the spectrum near ν_m can supply two other equations, namely, the equations for the peak frequency and for the peak flux (adding only one independent equation to the two equations for ν_a and $F_{\nu_a, \text{ext}}$). An additional independent equation is obtained for the cooling break frequency, ν_c . The power law, p , of the electron distribution can be determined from the high-energy slope ($\nu \gg \nu_m$). It is therefore possible with sufficient observational data to determine all the physical parameters of the afterglow: p , ϵ_e , ϵ_B , E_{52} , and n_1 . A similar calculation, using equations for ν_a , ν_m , F_{ν_m} , and ν_c , was made by Wijers & Galama (1999) for GRB 970508. In fact, the additional equation for $F_{\nu_a, \text{ext}}$ could result in an overconstrained system, which would provide a consistency check of the solution. The equation we obtained from ν_a differs by a factor of ~ 2 from the corresponding equation given in Wijers & Galama. This has a significant effect (up to a factor of ~ 17) on the values of the physical parameters of the burst that they give. We have shown (Table 1) that if other equations are corrected as well, the values of the physical parameters vary even more (up to 2 orders of magnitude). This stresses the sensitivity of this method to the exact details of the theoretical model of the spectrum.

We thank Ehud Cohen for useful discussions and Dale Frail and Shri Kulkarni for observational information. This research was supported by NASA grant NAG 5-3516, and a US-Israel Grant 95-328. Re'em Sari thanks the Clore Foundation for support.

APPENDIX

FORMALISM FOR THE B_{rad} AND B_{\perp} MODELS

The emission of a single electron, whose velocity makes an angle α with respect to the direction of the magnetic field B' in the local frame, is essentially into a cone with an opening angle α around the direction of the magnetic field (Rybicki &

Lightman 1979). The emission is almost completely into an opening angle $\Delta\theta \sim 1/\gamma_e$ around α (i.e., between cones with opening angles $\alpha \pm \Delta\theta$ about the direction of \mathbf{B}'). It is therefore a good approximation to take a δ function in the direction of the emission of a single electron,

$$j'_{\nu,e}(\gamma_e, \alpha, \theta'_B) = P'_{\nu,e}(\gamma_e, \alpha) \frac{\delta(\alpha - \theta'_B)}{2\pi \sin \alpha}, \quad (\text{A1})$$

where this is the emission in a direction making an angle θ'_B with the direction of \mathbf{B}' (in the local frame), and $P'_{\nu,e}$ is given by equation (6). Since we assume an isotropic electron velocity distribution in the local frame [$N(\gamma_e, \Omega_\alpha) = N(\gamma_e)/4\pi$], we obtain

$$j'_\nu(\theta'_B) = \frac{1}{4\pi} \int_{\gamma_{\min}}^{\infty} N(\gamma_e) d\gamma_e \int d\Omega_\alpha j'_{\nu,e}(\gamma_e, \alpha, \theta'_B) = \frac{1}{4\pi} \int_{\gamma_{\min}}^{\infty} N(\gamma_e) d\gamma_e P'_{\nu,e}(\gamma_e, \theta'_B), \quad (\text{A2})$$

where we have used equation (A1).

The angle of emission in the local frame is related to that in the observer frame by

$$\mu' = \frac{\mu - \beta}{1 - \beta\mu} \cong \frac{9\chi y^4 - 1}{1 + 7\chi y^4}, \quad (\text{A3})$$

and therefore

$$\sin^2 \theta' = 1 - \mu'^2 = \frac{32\chi y^4(1 - \chi y^4)}{(1 + 7\chi y^4)^2}. \quad (\text{A4})$$

For B'_{rad} , the magnetic field is in the radial direction, implying $\theta'_B = \theta'$. Since $P'_{\nu,e}(\gamma_e, \theta'_B) \propto \sin^{2/3} \theta'_B$ for $v \ll v_m$ (see eq. [6]), we take equation (A4) to the power of $1/3$ when substituting equation (6) into equation (A2) to obtain the emission coefficient for the B_{rad} model.

For the B_\perp model, it is assumed that the magnetic field is randomly oriented within the plane perpendicular to \hat{r} , in the local frame, with an equal probability for all directions ($0 \leq \varphi < 2\pi$) within this plane. We take the average value of $\sin^{2/3} \theta'_B$,

$$\langle \sin^{2/3} \theta'_B \rangle_\varphi = \frac{1}{2\pi} \int_0^{2\pi} d\varphi \sin^{2/3} \theta'_B = \frac{1}{2\pi} \int_0^{2\pi} d\varphi (1 - \sin^2 \theta' \sin^2 \varphi)^{1/3} = {}_2F_1(-1/3, 1/2, 1, \sin^2 \theta'), \quad (\text{A5})$$

where ${}_1F_2$ is the hypergeometric function, and $\sin^2 \theta'$ is given by equation (A4).

In order to obtain the absorption coefficient, α_ν , in terms of the emission, one uses the relations between the Einstein coefficients, which link emission and absorption on the most fundamental level. In doing so, we closely follow Rybicki & Lightman (1979), and use their notations, while generalizing for anisotropic absorption and emission. The relations between the Einstein coefficients per unit solid angle are

$$g_1 B_{12}(\Omega) = g_2 B_{21}(\Omega), \quad A_{21}(\Omega) = \frac{2h\nu^3}{c^2} B_{21}(\Omega), \quad (\text{A6})$$

where $A_{21}(\Omega)$, $B_{12}(\Omega)I_\nu$, and $B_{21}(\Omega)I_\nu$ are the transition probability per unit time per unit solid angle for spontaneous emission, absorption, and stimulated emission, respectively. These relations imply that all three coefficients have the same angular dependence,

$$A_{21}(\Omega)/A_{21} = B_{12}(\Omega)/B_{12} = B_{21}(\Omega)/B_{21} = f(\Omega), \quad \int f(\Omega) d\Omega = 1. \quad (\text{A7})$$

The emission and absorption coefficients for a given transition are given by

$$j_\nu(\Omega) = h\nu \sum_{E_1} \sum_{E_2} n(E_2) A_{21}(\Omega) \phi_{21}(\nu), \quad \alpha_\nu(\Omega) = h\nu \sum_{E_1} \sum_{E_2} [n(E_1) B_{12}(\Omega) - n(E_2) B_{21}(\Omega)] \phi_{21}(\nu). \quad (\text{A8})$$

Equations (A7) and (A8) imply that the source function, $S_\nu \equiv j_\nu/\alpha_\nu$, is always isotropic (independent of Ω). Furthermore, the value of the magnetic field does not effect S_ν , since j_ν and α_ν have the same dependence on B . We therefore expect that the flux density in the optically thick regime ($\nu \ll \nu_a$) should be independent of the magnetic field (as we indeed obtain for the magnetic field models we consider). This result should hold for any magnetic field, as long as the bulk of the observed image remains optically thick. The optical depth, on the other hand, does depend on the magnetic field model.

Following Rybicki & Lightman (1979, pp. 186–189), we obtain

$$\alpha_\nu(\Omega) = \frac{p+2}{2m_e v^2} \int_{\gamma_{\min}}^{\infty} d\gamma_e \int d\Omega_\alpha j_{\nu,e}(\gamma_e, \Omega, \alpha) \frac{N(\gamma_e, \Omega_\alpha)}{\gamma_e}. \quad (\text{A9})$$

Substituting equation (A1) and $N(\gamma_e, \Omega_\alpha) = N(\gamma_e)/4\pi$ (for an isotropic electron distribution), we obtain

$$\alpha'_\nu(\Omega) = \frac{p+2}{8\pi m_e v^2} \int_{\gamma_{\min}}^{\infty} d\gamma_e P'_{\nu,e}(\gamma_e, \theta'_B) \frac{N(\gamma_e)}{\gamma_e}. \quad (\text{A10})$$

In the B_{rad} and B_\perp models, the magnetic field strength assumes a fraction ϵ_B of its equipartition value just behind the shock front, and from there on evolves according to the “frozen-field” approximation. This implies (GPS) that the magnetic field for

these models is given by

$$B_{\text{rad}} = B'_{\text{eq}} \chi^{7/12}, \quad B_{\perp} = B'_{\text{eq}} \chi^{-7/24}, \quad (\text{A11})$$

respectively, where B'_{eq} is the magnetic field according to the equipartition model. Substituting equation (A11) and the appropriate average values of $\sin^{2/3} \theta'_B$ into equation (6), we obtain expressions for $P_{v',e}$, for the B_{rad} and B_{\perp} models. The absorption coefficient is then obtained using equation (A10):

$$\alpha'_{v'} = \frac{2^{14/3}(3\pi)^{2/3}}{\Gamma(1/3)} \frac{(p+2)(p-1)^{8/3}}{(3p+2)(p-2)^{5/3}} \frac{\epsilon_B^{1/3} n_0^{4/3} q_e^{8/3}}{\epsilon_e^{5/3} m_p^{4/3} c v'^{5/3}} \frac{y^{4/3} (1-7\chi y^4)^{1/3}}{\chi^{13/18} (1+7\chi y^4)^{2/3}} \quad (\text{A12})$$

for B_{rad} , and

$$\alpha'_{v'} = \frac{8(3\pi)^{2/3}}{\Gamma(1/3)} \frac{(p+2)(p-1)^{8/3}}{(3p+2)(p-2)^{5/3}} \frac{\epsilon_B^{1/3} n_0^{4/3} q_e^{8/3}}{\epsilon_e^{5/3} m_p^{4/3} c v'^{5/3}} \frac{{}_2F_1(-1/3, 1/2, 1, \sin^2 \theta')}{\chi^{59/36}} \quad (\text{A13})$$

for B_{\perp} , where $\sin^2 \theta'$ is given by equation (A4). The optical depth can be calculated in a similar manner as for B_{eq} , as shown in equation (19). For B_{rad} , it is given by

$$\tau(x, y) = \int \alpha_v ds = \frac{5\Gamma(5/6)2^{8/3}}{\sqrt{\pi}\Gamma(1/3)\phi^{5/3}} \int_y^{y_{\text{max}}(x)} dy \frac{y^3 [1-7\chi(x, y)y^4]^{1/3}}{\chi^{7/18}(x, y) [1+7\chi(x, y)y^4]^{4/3}} \quad (\text{A14})$$

and is shown in Figure 8. In a similar manner as employed for B_{eq} in § 3, we obtain dimensionless radiative transfer equations for B_{rad} ,

$$\frac{d\tilde{I}_v}{dy} = \frac{20\Gamma(5/6)2^{2/3}y^3(1-\chi y^4)^{1/3}}{\sqrt{\pi}\Gamma(1/3)\phi^{5/3}\chi^{7/18}(1+7\chi y^4)^{4/3}} \left(\frac{8y\chi^{1/3}}{1+7\chi y^4} - \tilde{I}_v \right), \quad (\text{A15})$$

and for B_{\perp} ,

$$\frac{d\tilde{I}_v}{dy} = \frac{10\Gamma(5/6)y^{5/3}{}_2F_1(-1/3, 1/2, 1, \sin^2 \theta')}{\sqrt{\pi}\Gamma(1/3)\phi^{5/3}\chi^{47/36}(1+7\chi y^4)^{2/3}} \left(\frac{8y\chi^{1/3}}{1+7\chi y^4} - \tilde{I}_v \right). \quad (\text{A16})$$

REFERENCES

- Blandford, R. D., & McKee, C. F. 1976, *Phys. Fluids*, 19, 1130
 Brainerd, J. J. 1997, *ApJ*, 496, L67
 ———. 1998, in *Fourth Gamma-Ray Burst Symp.*, ed. C. A. Meegan, R. D. Preece, & T. M. Koshut (New York: AIP), 727
 Frail, D. A., et al. 1997, *Nature*, 389, 261
 Granot, J., Piran, T., & Sari, R. 1999, *ApJ*, 513, 679
 Gruzinov, A., & Waxman, E. 1999, *ApJ*, 511, 852
 Katz, J. 1994, *ApJ*, 422, 248
 Katz, J., & Piran, T. 1997, *ApJ*, 490, 772
 Kobayashi, S., Piran, T., & Sari, R. 1999, *ApJ*, 513, 669
 Medvedev, M. V., & Loeb, A. 1999, preprint (astro-ph/9904363)
 Panaitescu, A., & Mészáros, P. 1998, *ApJ*, 493, L31
 Rybicki, G. B., & Lightman, A. P. 1979, *Radiative Processes in Astrophysics* (New York: Wiley-Interscience)
 Sari, R. 1997, *ApJ*, 489, L37
 ———. 1998, *ApJ*, 494, L49
 Sari, R., Piran, T., & Narayan, R. 1998, *ApJ*, 497, L17
 Shepherd, D. S., et al. 1998, *ApJ*, 497, 859
 Taylor, G. B., et al. 1998, *ApJ*, 502, L115
 Waxman, E. 1997a, *ApJ*, 485, L5
 ———. 1997b, *ApJ*, 489, L33
 ———. 1997c, *ApJ*, 491, L19
 Wijers, R. A. M. J., & Galama, T. J. 1999, *ApJ*, 523, 177
 Wijers, R. A. M. J., Rees, M. J., & Mészáros, P. 1997, *MNRAS*, 228, L51